

Predicting tuberculosis drug resistance with machine learning-assisted Raman spectroscopy

Authors: Babatunde Ogunlade^{1*†}, Loza F. Tadesse^{2,3,4*†}, Hongquan Li^{5*†}, Nhat Vu⁶, Niaz Banaei⁷, Amy K. Barczak^{4,8,9}, Amr. A. E. Saleh^{1,10}, Manu Prakash² and Jennifer A. Dionne^{1,11†}

Affiliations:

¹ Department of Materials Science and Engineering, Stanford University; Stanford, 94305, CA, USA.

² Department of Bioengineering, Stanford University School of Medicine and School of Engineering; Stanford, 94305, CA, USA.

³ Department of Mechanical Engineering, Massachusetts Institute of Technology; Cambridge, 02142, MA, USA.

⁴ The Ragon Institute, Massachusetts General Hospital; Cambridge, 02139, MA, USA.

⁵ Department of Applied Physics, Stanford University; Stanford, 94305, CA, USA.

⁶ Pumpkinseed Technologies, Inc; Palo Alto, 94306, CA, USA.

⁷ Department of Pathology, Stanford University School of Medicine; Stanford, 94305, CA, USA.

⁸ Division of Infectious Diseases, Massachusetts General Hospital; Boston, 02114, MA, USA.

⁹ Department of Medicine, Harvard Medical School; Boston, 02115, MA, USA.

¹⁰ Department of Engineering Mathematics and Physics, Cairo University; Giza, 12613, Egypt.

¹¹ Department of Radiology, Molecular Imaging Program at Stanford (MIPS), Stanford University School of Medicine; Stanford, 94035, CA, USA.

*Indicates equal contribution

† To whom correspondence should be addressed;

E-mail: bogun@stanford.edu; hqli@stanford.edu; lozat@mit.edu; jdionne@stanford.edu.

One Sentence Summary: Raman spectroscopy and machine learning can be used to rapidly identify and differentiate strains of antibiotic-resistant tuberculosis (TB) with high accuracy, on a low-cost platform suitable for deployment in TB-endemic regions.

Abstract:

Tuberculosis (TB) is the world's deadliest infectious disease, with 1.5 million annual deaths and half a million annual infections. Rapid TB diagnosis and antibiotic susceptibility testing (AST) are critical to improve patient treatment and to reduce the rise of new drug resistance. Here, we develop a rapid, label-free approach to identify *Mycobacterium tuberculosis* (Mtb) strains and

antibiotic-resistant mutants. We collect over 20,000 single-cell Raman spectra from isogenic mycobacterial strains each resistant to one of the four mainstay anti-TB drugs (isoniazid, rifampicin, moxifloxacin and amikacin) and train a machine-learning model on these spectra. On dried TB samples, we achieve > 98% classification accuracy of the antibiotic resistance profile, without the need for antibiotic co-incubation; in dried patient sputum, we achieve average classification accuracies of ~ 79%. We also develop a low-cost, portable Raman microscope suitable for field-deployment of this method in TB-endemic regions.

Main text:

INTRODUCTION

The discovery of antibiotics in the early 20th century marked a turning point in our defense against tuberculosis (TB) – one of the deadliest infectious diseases known to humans. At that time, TB had become curable and was considered to be on a path toward elimination. However, by the end of the 20th century, TB re-emerged as a leading cause of death globally, in part due to challenges in diagnosis and its evolved resistance to antibiotics. While growth in liquid culture is considered the gold standard for organism identification and determination of antibiotic susceptibility, the causative organism, *Mycobacterium tuberculosis* (Mtb) can take up to 40 days to culture. As antibiotic susceptibility testing requires pathogen growth, definitive determination of Mtb antibiotic resistance using traditional antibiotic susceptibility testing (AST) can take additional weeks. In the delay between diagnosis and AST results, many patients are treated with only partially active antibiotic regimens, giving rise to resistant strains. In 2021 alone, more than half a million cases of multidrug resistant TB infections were reported (1).

To mitigate the rise of antimicrobial resistance, a key strategy of the World Health Organization (WHO) is to improve surveillance of antibiotic-resistant infections, and to promote the appropriate use of quality medicines (2). To address WHO guidelines, several culture-free AST approaches are being developed. For example, nucleic acid amplification tests and polymerase chain reaction (PCR) do not require culturing and are highly sensitive and specific. However, these tests are limited to identifying resistance in cases in which a defined number of known genomic mutations confer resistance (e.g., the *rpoB* gene for resistance to rifampicin (3)). These assays also require multiple reagents, can suffer from errors with each thermal cycle, and cannot distinguish between live and dead bacteria, so they cannot be used to monitor treatment efficacy. Further, these assays cost well above the targeted \$5000 in capital cost specified by the WHO for next generation TB drug-susceptibility testing tools (4). Complementing PCR, loop-mediated isothermal amplification (LAMP) assays eliminate the need for thermal cycling. However, these LAMP assays cannot detect mutations in resistance-associated genes because of their inability to resolve single-nucleotide differences (5). Rapid lateral flow point-of-care test antigen/antibody detection methods provide simpler and faster alternatives to LAMP and PCR but have poor sensitivity and specificity. There is also a significant delay in the appearance of target antigens in sputum or antibodies in the bloodstream, and these antigens do not necessarily indicate Mtb drug susceptibility. Therefore, current AST methods do not collectively provide the speed, sensitivity, and specificity needed in one system to meet WHO's goals for drug-resistant TB eradication.

As an up-and-coming approach, Raman spectroscopy has the potential to identify the antibiotic resistance profiles of bacteria at the single-cell level using acquisition times on the order of

seconds. Raman spectroscopy utilizes inelastic light scattering to probe the vibrational modes of a sample as a fingerprint. Different bacterial phenotypes are characterized by unique biomolecular compositions, leading to subtle differences in their corresponding Raman spectra. The Raman spectra of biological macromolecules typically reside between 500 and 1900 cm^{-1} , with lipids, proteins, and nucleic acids exhibiting fingerprints between 1000-1700 cm^{-1} , 1200-1660 cm^{-1} , and 600-1100 cm^{-1} , respectively (6). As such, these unique Raman spectral signatures can be used for accurate cellular detection, identification, and antibiotic susceptibility testing. Using Raman spectroscopy and machine learning (ML) based spectral analysis, we have previously shown that genetically engineered antibiotic resistant and susceptible *S. aureus* strains can be classified with ~89% accuracy (7). Similarly, we and others have used machine learning-assisted Raman to identify over 31 bacterial species and strains (7,8, 9), including pathogens in liquid solvents (10) and in blood (11, 12); to identify substrains of *E.coli* (13, 14), to identify various respiratory viruses (15), to identify various cellular metabolites and secretomes (16), to assess the effects of antibiotics on resistant and susceptible bacteria (17, 18), and to determine *S. aureus* antibiotic susceptibility without co-incubation (19). Despite these pioneering studies, determination of antibiotic susceptibility of TB, and methods translation to TB-endemic regions, remains an outstanding, untackled challenge.

Here, we demonstrate a rapid, culture-free, and antibiotic co-incubation free antibiotic susceptibility test for TB, based on the integration of Raman spectroscopy and machine learning. Particularly, we classify the antibiotic resistance profile of 5 isogenic Bacillus Calmette-Guérin (BCG) strains using a convolutional neural network. We collect Raman spectra from over 20,000 individual cells resistant to one of the four mainstay anti-TB drugs (isoniazid, rifampicin, moxifloxacin and amikacin) and a pan-susceptible wild type strain. Using only 15-second integration times and Raman features from across the entire spectral range (740-1802 cm^{-1}), we achieve >98% resistant versus susceptible classification accuracy across all 5 BCG strains. In addition, we show that various genetic mutants can be accurately classified according to their antibiotic resistance. Using feature recognition algorithms, we also identify the subsets of wavenumbers which most strongly influence antibiotic resistance classification. These algorithms show that antibiotic resistance behavior is primarily reflected in certain vibrational modes – particularly those of mycolic acid - that underlie the molecular-level antibiotic response of the bacteria. These algorithms also show that targeting the entire spectral range of scientific grade Raman instruments is not necessary for TB AST. To this end, we develop a low-cost portable Raman setup that targets select wavenumber bands, for point-of-care applications. Our instrument costs <\$5000, and with inclusion of plasmonic nanoantennas for surface-enhanced Raman spectroscopy (SERS), achieves an average accuracy of 89% across all 5 BCG strains. In dried patient sputum samples, our instrument achieves ~79% classification accuracy – providing a foundation for rapid, low-cost, and portable AST testing in resource-limited regions.

RESULTS

Single-cell Raman spectroscopy of Mtb for antibiotic incubation-free drug testing

As summarized in Figure. 1, we deposit mycobacterial cells onto gold-coated silica substrates and collect single-cell Raman spectra (Fig. 1A). For our studies, we controllably engineer antibiotic-resistant Mtb models using BCG, a live-attenuated form of *Mycobacterium Bovis* as a model organism. While lacking central virulence determinants, BCG is nearly identical to Mtb in its core bacterial functions, including DNA replication, RNA polymerase, and cell wall

functions. We use these models to enable safe handling of resistant samples in BSL-2 facilities for the proof-of-concept studies performed here. Individual Raman spectra are used as an input into our convolutional neural network; we employed a 10-fold cross validation scheme to determine the unbiased model performance. The output of this algorithm is a series of probability scores for antibiotic resistance (Fig. 1B). The class with the highest probability score is chosen as the predicted class.

We performed our antibiotic susceptibility test on five isogenic BCG strains: those resistant to the first-line TB antibiotics isoniazid and rifampicin; those resistant to the second-line TB antibiotics moxifloxacin and amikacin; and also on a fully antibiotic-susceptible control strain (hereby described as wildtype). Figure 1C shows the minimum inhibitory concentration of the four anti-TB antibiotics used on our five BCG strains, confirming each resistant strain's resistance to a single antibiotic as well as the full antibiotic susceptibility of the wildtype strain. As seen in Figures 1D-H, scanning electron micrographs show no distinct morphological difference among the resistant strains.

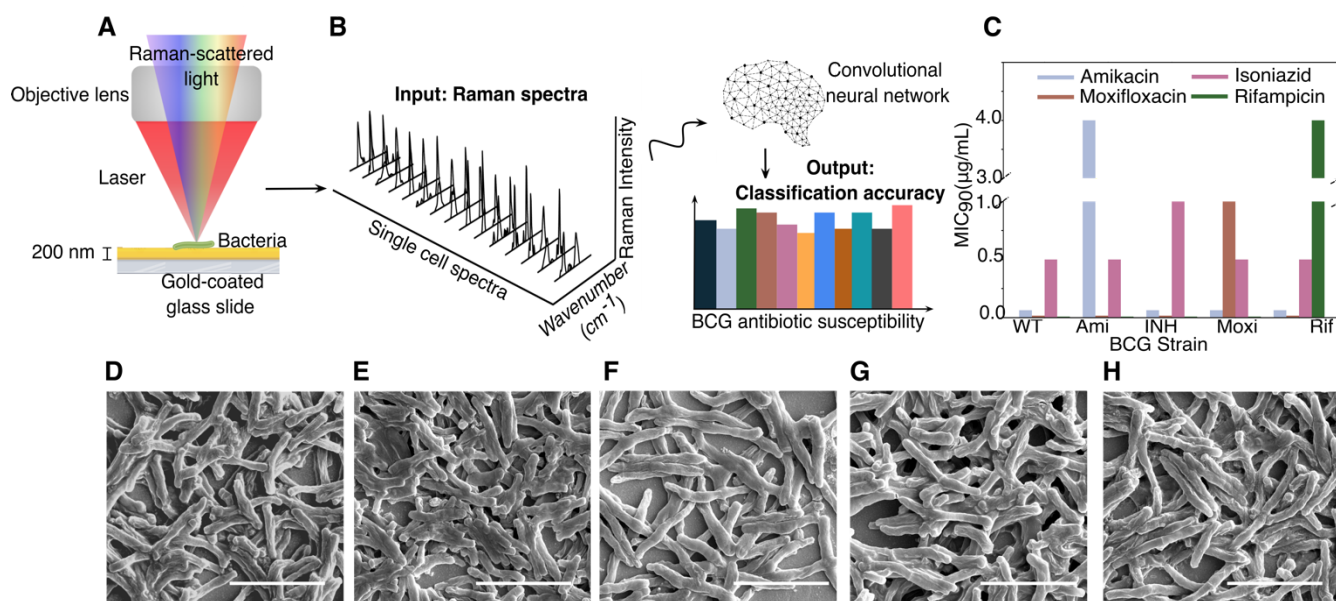


Figure 1. Experimental setup and example bacterial Raman spectra with antibiotic resistance profiles. A) Diffraction-limited spot of a 633 nm incident laser collecting a spectrum from roughly a single bacterial cell. B) Bacterial spectra are used as input for the neural network to perform a classification task that outputs probability scores for each bacterium antibiotic resistance. C) Minimum inhibitory concentrations for the five distinct strains tested across the four main antibiotics using standard serial two-fold dilution. See Table S1 for details. (D, E, F, G) Scanning electron microscopy (SEM) image of a monolayer of wildtype, amikacin-resistant, rifampicin-resistant, isoniazid-resistant, and moxifloxacin-resistant BCG. Scale bar is 4 µm.

As shown in Fig. 2A, the average Raman spectra of the 5 distinct BCG strains (~ 1700 spectra per strain) look similar, with major spectral peaks preserved across the strains. However, there are some noticeable differences in the ~1000, ~1300, ~1500 and ~1700 cm^{-1} bands between wildtype and four resistant strains; the majority of these vibrational modes correspond to cell-wall components such as mycolic acid and proteins. Therefore, the differences between the spectra are most likely due to differences in cell-wall composition and structure, discussed later

in the text. We performed t-distributed stochastic neighbor embedding (t-SNE) which shows significant clustering for each of the 5 strains (Fig. 2B). Such clustering suggests that accurate classification by resistance should be possible. To classify the antibiotic resistance profiles of the 5 BCG strains, we developed a deep learning model, a ResNet (20) variant (7). We perform a stratified K-fold cross validation of our convolutional neural network's performance across 10 splits. As seen in Figure 2C, we achieve an average accuracy of 98% across all BCG strains. Note that main diagonal elements represent correct classifications and off-diagonal elements represent misclassifications. High classification accuracies were also obtained with different gold-coated glass slide substrates (Fig. S3). These results demonstrate that our approach is agnostic to the particular substrate selected or batch effects and are solely from intrinsic differences in the strains themselves. Therefore, Raman spectroscopy in conjunction with machine learning can be used to predict antibiotic resistance in mycobacteria without the need for antibiotic co-incubation and hence without culturing.

Select spectral bands are most crucial for predicting antibiotic resistance

We quantitatively identify the regions of the spectra that are key for the high classification accuracy. To identify these meaningful bands, we used a probing algorithm that perturbs the input data before re-running the classification through the trained models from Fig. 2C (21). Using each test fold from our 10-fold cross validation, we iterate through the wavenumbers and at each iteration, perturb the spectrum by modulating the amplitude of the spectral intensity with a Voigt distribution centered at the probing wavenumber. After each perturbation, we recalculate the classification accuracy, compare the updated results with our baseline classification accuracy, and determine the importance for each wavenumber - the greater the decrease in accuracy due to a given perturbation, the more important the wavenumber. As shown in Fig. 2D, these regions are spectral bands located around 1295, 1437 and 1660 cm^{-1} (22). These wavenumber bands correspond to mycolic acid $-\text{CH}_2$ twist and $-\text{CH}_2$ deformation modes, and Amide I $\text{C}=\text{O}$ stretching modes, which change when the bacteria develop resistance. It is known that single point mutations in relevant genes confer resistance to a given anti-TB drug, such as the GyrA or GyrB genes in moxifloxacin-resistant Mtb as well as the katG gene in isoniazid-resistant Mtb. Therefore, our analysis suggests that the biochemical origins of resistance can be tracked by examining important features in the Raman spectra.

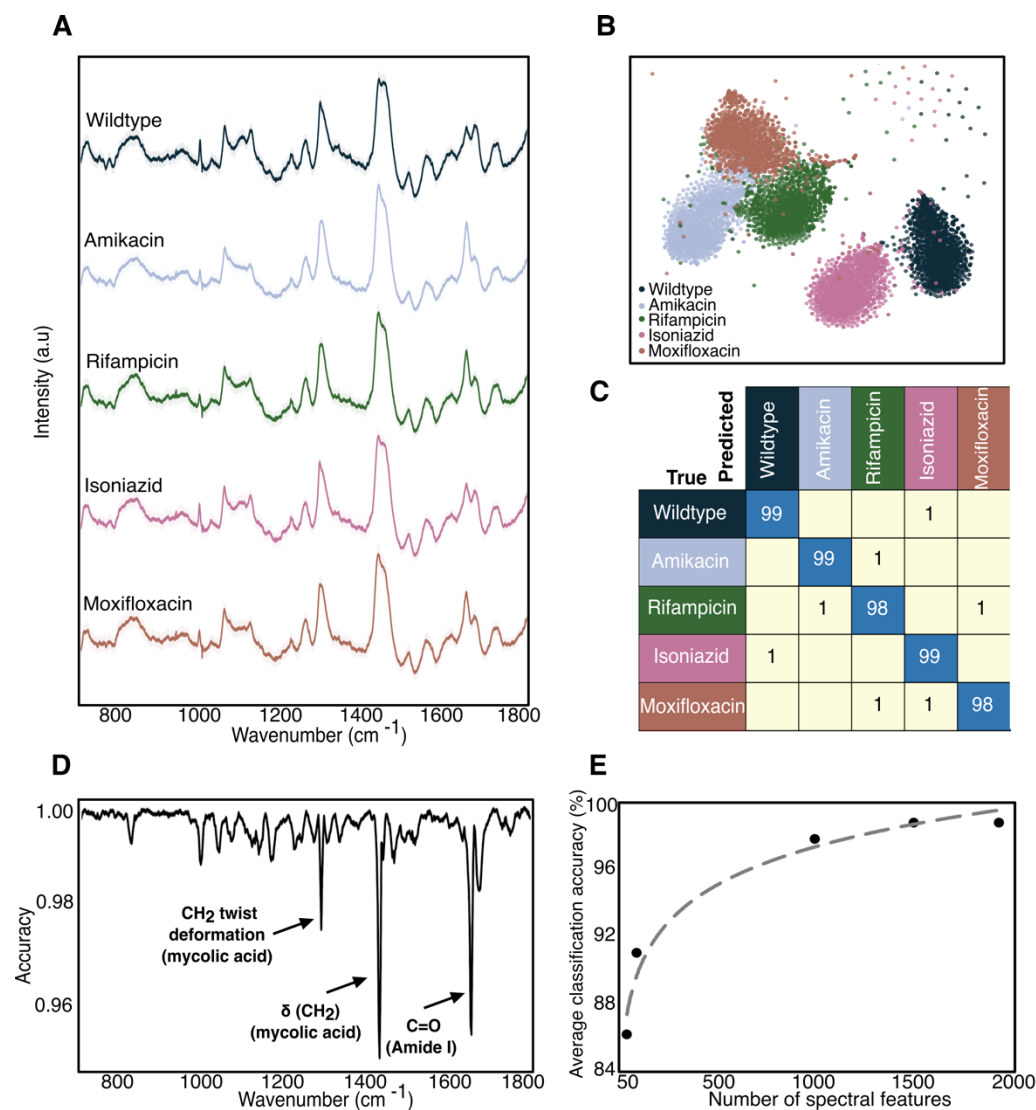


Figure 2. BCG antibiotic resistance determination. A) Average spectrum with standard deviation of all spectrograms (1700 spectra collected at 15s acquisition) from the 5 BCG strains. The spectra show significant differences in both peak position and peak intensity at bands centered at $\sim 1000 \text{ cm}^{-1}$, 1060 cm^{-1} , and between $\sim 1300\text{-}1700 \text{ cm}^{-1}$. B) Two-dimensional t-SNE projection across all Raman spectra of the dataset for 5 BCG samples susceptible and resistant to the four different antibiotics tested grouped according to antibiotic class showing clustering. C) Normalized confusion matrix generated using CNN on the single-cell spectra collected from 5 BCG strains, grouped by antibiotic class. Samples were evaluated by performing a stratified K-fold cross validation of our classifier's performance across 10 splits, showing $\sim 98\%$ classification accuracy across all samples. D) Feature selection highlighting the identification of true, physical vibrational modes. Feature selection performed to determine relative weight of spectral wavenumbers in our CNN classification. E) Average classification accuracy as a function of the number of top spectral features selected showing 96% accuracy with only 500 features.

Next, we reduced the wavenumber feature input to our neural network, reflecting those bands most important for high-accuracy classification. Using only the top 50 wavenumbers, we achieve $\sim 86\%$ accuracy. Classification accuracy increases to 96% when using 250 features, and further to 98% when using all 1930 features (Fig. 2E). This result indicates potential for use of a cost-effective spectrometer, compared to the scientific grade tool, targeting these select bands; we use this insight to design our low-cost Raman microscope, discussed later in the text.

Antibiotic-resistant mutants can be accurately classified

To test the robustness of our approach to genetic mutations, we interrogated four isoniazid-resistant mutants and three amikacin-resistant mutants. As seen in Figure 3A, the isoniazid-resistant mutants differ from each other by single point mutations in the *katG* gene, which encodes for catalase peroxidase, an enzyme that converts isoniazid to its biologically active form (23). Isoniazid resistant mutant 1 has a single point mutation at position 609 from cytosine to thymine; isoniazid resistant mutant 2 has two single point mutations at positions 290 and 609 from adenine to guanine and cytosine to thymine, respectively; isoniazid resistant mutant 3 has a single point mutation at position 1292 from guanine to adenine; and isoniazid resistant mutant 4 has no single point mutations identified in *katG*, and likely harbors a non-*katG* mutation conferring the observed isoniazid resistance. As seen in Figure 3B, Raman spectra from these distinct isoniazid-resistant mutants are seemingly identical, with tightly overlapping projections on t-SNE clustering (Fig. 3C). Yet, there is slight separability within the mutant clusters, suggesting that Raman spectroscopy could have the remarkable ability to predict point mutations in the genetic sequence of pathogens, and possibly other cells.

The three amikacin-resistant mutants reveal similar clustering on the t-SNE projection. Importantly, however, the clustering is distinct from the isoniazid cluster. The classification accuracy to predict the antibiotic susceptibility of each strain within its antibiotic class is ~99% (Fig. S2). Clinically, this result is significant, as it is likely that antibiotic-resistant mutants from different patients will differ on the single nucleotide scale, and we are able to identify resistance to a particular antibiotic regardless of this difference.

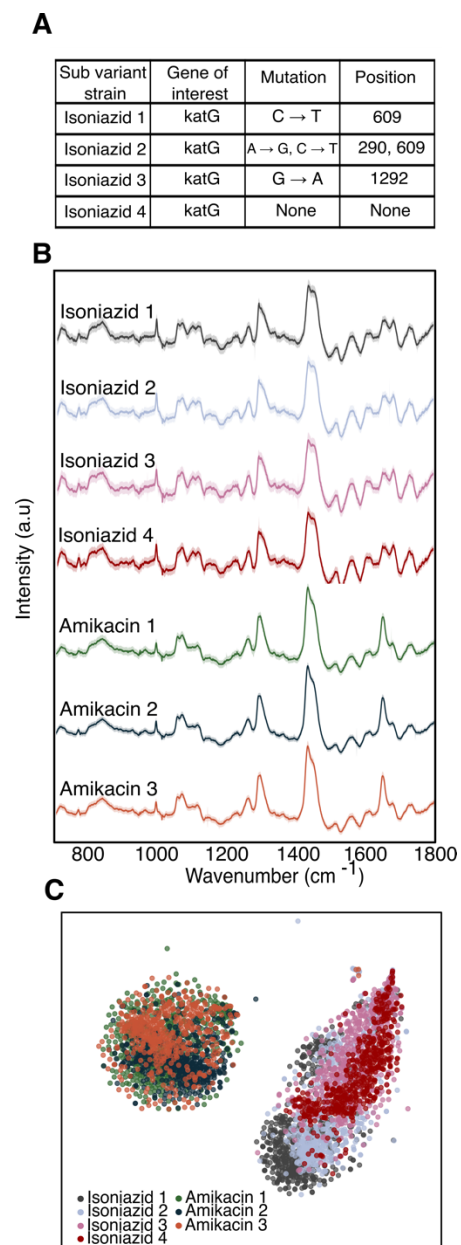


Figure 3. Resistant mutant prediction. A) Sequencing results showing single mutation differences resulting in mutants of resistant strains against isoniazid and amikacin B) Average Raman spectra of 529 single cell spectra with standard deviation of four isoniazid resistant mutants and three amikacin-resistant mutants showing nearly identical fingerprints among their respective class of resistance. C) t-SNE plot showing overlapping clusters of mutants within a class of antibiotic resistance.

Enabling low-cost and portable Raman for Mtb drug testing

To demonstrate that our findings can translate to point-of-care TB drug testing in resource-limited regions, we developed a low-cost, portable, and fully automated Raman microscope (Fig. 4A). This Raman microscope is based on the Octopi/Squid modular microscope framework developed by our team for fluorescence (24, 25, 26), but advances this setup for spectroscopy. The instrument utilizes a non-cooled CMOS camera (Sony IMX290), a transmission diffraction grating with >95% efficiency, and a design without a pinhole or slit for low-cost spectroscopy. A fiber-coupled 785 nm VHG-stabilized laser is used as the excitation

source. To boost the signal from single bacteria, we synthesize gold nanoparticles (AuNPs) for surface-enhanced Raman scattering. As seen in Figure 4B, these nanorods have a scattering resonance near the pump-laser wavelength. Compared to whole-cell Raman, these nanorods yield a ~ 2 order of magnitude increase in Raman scattering (9, 10, 11, 27, 28, 29, 30, 31) from single cells and pathogens and considerably shorten the integration times required for single-cell analysis on our microscope. The AuNPs are also relatively inexpensive to synthesize or purchase, easy to tune optically (32, 33, 34) and easy to integrate with our bacterial strains. All components combined for this microscope and spectrometer are $< \$5000$. Additional details on the sample preparation and imaging/spectroscopy are provided in SI.

As a baseline measurement, we first collected ~ 3000 spectra from the 5 BCG strains mixed with gold nanorods using 0.3 second integration times and 3 accumulations per sample (Fig. 4B). Here, the shortened integration time was chosen to maintain a similar signal-to-noise ratio of the signal as with the Raman of the scientific-grade instrument. Similar to the spectra collected on the scientific grade Raman microscope in Fig. 2A, the average Raman spectra of the 5 distinct BCG strains look similar, with major spectral peaks preserved across the strains. However, there are some noticeable differences in the ~ 1000 , ~ 1300 and ~ 1400 cm^{-1} bands between wildtype and four resistant strains (Fig. 4D). We performed t-SNE which shows significant clustering for each of the 5 strains (Fig. 4E). As seen in Figure 4f, we achieve an average accuracy of 89% across all 5 BCG strains, comparable with the ~ 95 - 98% average classification accuracy achieved on our scientific-grade tool.

As an initial evaluation of the performance for clinical samples, we spiked BCG pathogens into sputum (see Methods), mixed the sample with gold nanorods, and collected a total of ~ 5300 spectra from the BCG strains. Using only 0.3 second integration times and 3 accumulations per sample, we obtain an average classification accuracy of $\sim 79\%$ for the 5 strains across two separate sputum samples (Fig. 4I and Fig. S7). This specificity is comparable with that observed for bacteria alone on scientific grade Raman instruments (Fig. 2C) while providing rapid results at a lower cost and smaller footprint.

We note that the spectra differ from those without using AuNPs, which is as expected as now the Raman signatures primarily originate from the surface-bound molecules on the bacteria, due to the electric field localization of the AuNPs. This intraclass spectral variation is evident in the milder, less intense clustering of the 5 strains in the t-SNE in Figure 4E and Figure 4H compared to the whole-cell Raman collected in Figure 2B. However, our convolution neural network can still classify strains, as demonstrated by the high accuracy we are able to obtain. Future work spanning more patient data and optimized spectral data processing could enable clinical BCG strain classification.

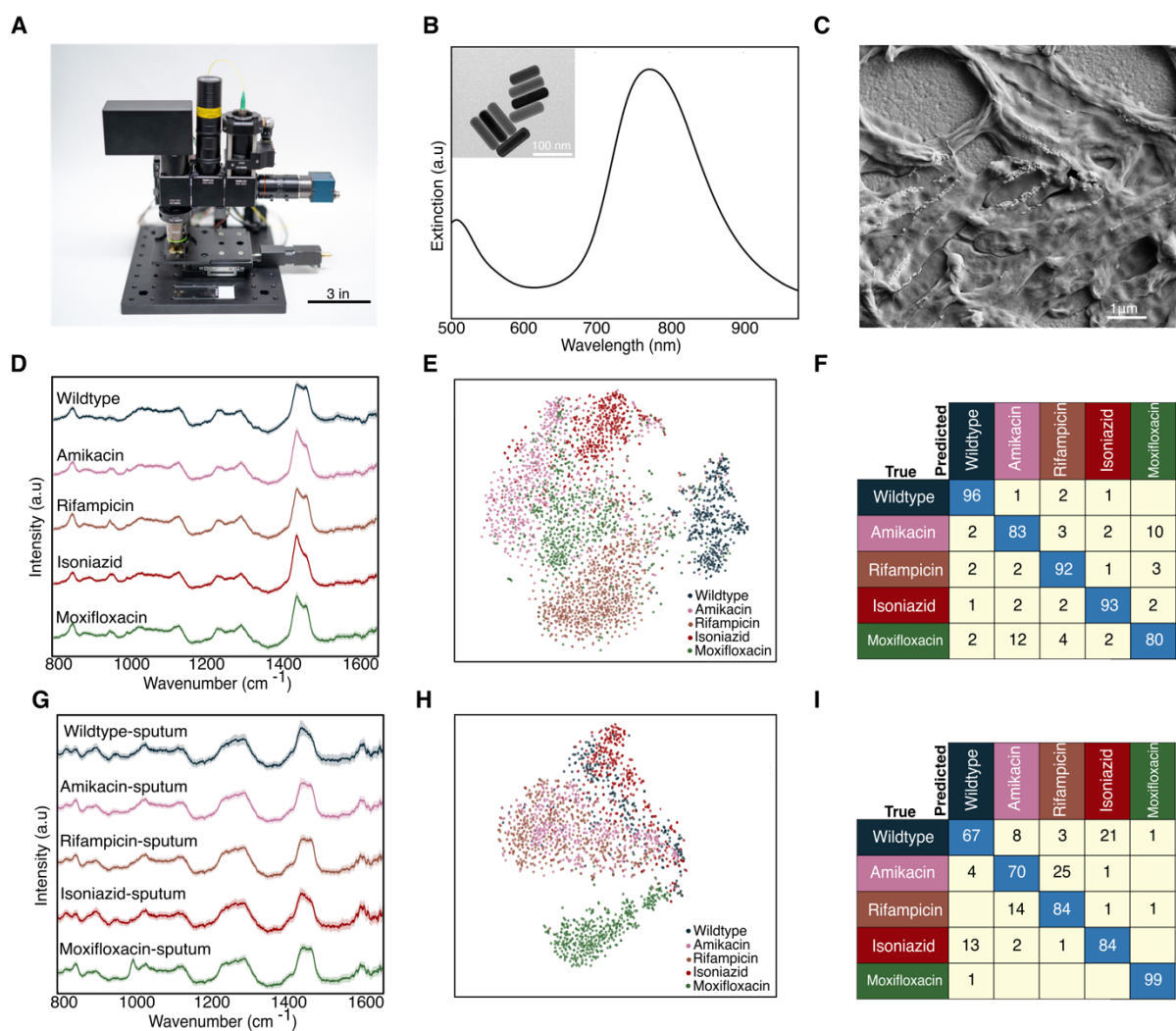


Figure 4. Demonstration on our low-cost Raman system. A) Photo of our system showcasing its small footprint and portable platform for use at the point-of-care. A standard microscope slide is included for scale. B) Extinction spectra of gold nanorods showing plasmon resonance centered at ~ 780 nm to overlap with the setup's 785 nm excitation laser. Panel (B) inset shows transmission electron micrograph of gold nanorods used. C) Scanning electron micrograph of BCG mixed with gold nanorods, which increase the Raman scattering from single cells. D) Raman spectra of the 5 BCG strains mixed with gold nanorods imaged on our setup. E) t-SNE projection across all Raman spectra of the 5 BCG strains. F) Average accuracy of $\sim 89\%$ is achieved using spectra from bacteria suspended in water and dropcast dried (replication of Fig. 2c on our setup) G) Raman spectra of the 5 BCG strains spiked in sputum imaged on our setup. H) t-SNE projection across all spiked sputum samples. I) Average accuracy of $\sim 79\%$ is achieved using spectra collected from two separate spiked sputum samples

DISCUSSION

In summary, we demonstrate a rapid and accurate TB AST methodology that is antibiotic co-incubation free and culture-free. Unlike current culture-based and nucleic acid amplification-based testing (NAATs) platforms, our Raman approach does not require lengthy culturing, expensive reagents, or thermal cycling equipment, and is robust to single nucleotide point mutations. Our approach can accurately classify resistance across a variety of antibiotics, and across a variety of genetic mutations. In addition, our machine learning models not only provide accurate AST classification, but also interpretability to the Raman spectra. Indeed, as

highlighted by our feature-recognition algorithms, resistance behavior is primarily reflected in certain vibrational modes, particularly those of mycolic acid, that underlie the molecular-level antibiotic response of the bacteria. By focusing on the wavenumbers most important for Mtb AST, we developed a low-cost portable Raman microscope, capable of high Mtb classification accuracy on dried samples and in dried sputum. On-going work is aimed at testing our approach in the field on Mtb-positive patients. Such clinical work will elucidate the intrinsic differences between strain types, well beyond sputum-to-sputum variations. If successful, this clinical work will provide a new and needed approach to enable the TB surveillance and diagnostic milestones set by the WHO.

References and notes

1. *Global tuberculosis report 2022* (World Health Organization, 2022).
2. G. T. Programme, WHO consolidated guidelines on tuberculosis: module 3: diagnosis: rapid diagnostics for tuberculosis detection, 2021 update (2021), (available at <https://www.who.int/publications/i/item/9789240029415>).
3. S. D. Lawn, P. Mwaba, M. Bates, A. Piatek, H. Alexander, B. J. Marais, L. E. Cuevas, T. D. McHugh, L. Zijenah, N. Kapata, I. Abubakar, R. McNerney, M. Hoelscher, Z. A. Memish, G. B. Migliori, P. Kim, M. Maeurer, M. Schito, A. Zumla, Advances in tuberculosis diagnostics: the Xpert MTB/RIF assay and future prospects for a point-of-care test. *The Lancet Infectious Diseases*. **13** (2013), pp. 349–361.
4. W. H.-P. T. P. Profiles, for New Tuberculosis Diagnostics: Report of a Consensus Meeting. *Geneva: World Health Organisation* (2014).
5. M. Varona, J. L. Anderson, Advances in Mutation Detection Using Loop-Mediated Isothermal Amplification. *ACS Omega*. **6**, 3463–3469 (2021).
6. D. W. Shipp, F. Sinjab, I. Notingher, Raman spectroscopy: techniques and applications in the life sciences. *Adv. Opt. Photonics*. **9**, 315 (2017).
7. C.-S. Ho, N. Jean, C. A. Hogan, L. Blackmon, S. S. Jeffrey, M. Holodniy, N. Banaei, A. A. E. Saleh, S. Ermon, J. Dionne, Rapid identification of pathogenic bacteria using Raman spectroscopy and deep learning. *Nat. Commun.* **10**, 4927 (2019).
8. S. Stöckel, S. Meisel, B. Lorenz, S. Kloß, S. Henk, S. Dees, E. Richter, S. Andres, M. Merker, I. Labugger, P. Rösch, J. Popp, Raman spectroscopic identification of *Mycobacterium tuberculosis*. *J. Biophotonics*. **10**, 727–734 (2017).
9. A. A. Moawad, A. Silge, T. Bocklitz, K. Fischer, P. Rösch, U. Roesler, M. C. Elschner, J. Popp, H. Neubauer, A Machine Learning-Based Raman Spectroscopic Assay for the Identification of *Burkholderia mallei* and Related Species. *Molecules*. **24** (2019), doi:10.3390/molecules24244516.
10. L. F. Tadesse, C.-S. Ho, D.-H. Chen, H. Arami, N. Banaei, S. S. Gambhir, S. S. Jeffrey, A. A. E. Saleh, J. Dionne, Plasmonic and Electrostatic Interactions Enable Uniformly Enhanced Liquid Bacterial Surface-Enhanced Raman Scattering (SERS). *Nano Lett.* **20**, 7655–7661 (2020).
11. F. Safir, N. Vu, L. F. Tadesse, K. Firouzi, N. Banaei, S. S. Jeffrey, A. A. E. Saleh, B. P. T. Khuri-Yakub, J. A. Dionne, Combining Acoustic Bioprinting with AI-Assisted Raman Spectroscopy for High-Throughput Identification of Bacteria in Blood. *Nano Lett.* (2023), doi:10.1021/acs.nanolett.2c03015.
12. S. Khan, R. Ullah, A. Khan, R. Ashraf, H. Ali, M. Bilal, M. Saleem, Analysis of hepatitis B virus infection in blood sera using Raman spectroscopy and machine learning. *Photodiagnosis Photodyn. Ther.* **23**, 89–93 (2018).

13. E. Kastanos, A. Kyriakides, K. Hadjigeorgiou, C. Pitris, A novel method for bacterial UTI diagnosis using Raman spectroscopy. *International Journal of spectroscopy*. **2012** (2012) (available at <https://www.hindawi.com/archive/2012/195317/abs/>).
14. A. Germond, T. Ichimura, T. Horinouchi, H. Fujita, C. Furusawa, T. M. Watanabe, Raman spectral signature reflects transcriptomic features of antibiotic resistance in *Escherichia coli*. *Communications Biology*. **1**, 85 (2018).
15. J. Ye, Y.-T. Yeh, Y. Xue, Z. Wang, N. Zhang, H. Liu, K. Zhang, R. Ricker, Z. Yu, A. Roder, N. Perea Lopez, L. Organtini, W. Greene, S. Hafenstein, H. Lu, E. Ghedin, M. Terrones, S. Huang, S. X. Huang, Accurate virus identification with interpretable Raman signatures by machine learning. *Proc. Natl. Acad. Sci. U. S. A.* **119**, e2118836119 (2022).
16. J. Plou, P. S. Valera, I. García, D. Vila-Liarte, C. Renero-Lecuna, J. Ruiz-Cabello, A. Carracedo, L. M. Liz-Marzán, Machine learning-assisted high-throughput SERS classification of cell secretomes. *Small*, e2207658 (2023).
17. A. N. Rousseau, N. Faure, F. Rol, Z. Sedaghat, J. Le Galudec, F. Mallard, Q. Josso, Fast Antibiotic Susceptibility Testing via Raman Microspectrometry on Single Bacteria: An MRSA Case Study. *ACS Omega*. **6**, 16273–16279 (2021).
18. W. R. Premasiri, Y. Chen, P. M. Williamson, D. C. Bandarage, C. Pyles, L. D. Ziegler, Rapid urinary tract infection diagnostics by surface-enhanced Raman spectroscopy (SERS): identification and antibiotic susceptibilities. *Anal. Bioanal. Chem.* **409**, 3043–3054 (2017).
19. B. L. Thomsen, J. B. Christensen, O. Rodenko, I. Usenov, R. B. Grønnemose, T. E. Andersen, M. Lassen, Accurate and fast identification of minimally prepared bacteria phenotypes using Raman spectroscopy assisted by machine learning. *Sci. Rep.* **12**, 16436 (2022).
20. K. He, X. Zhang, S. Ren, J. Sun, "Deep residual learning for image recognition" in *Proceedings of the IEEE conference on computer vision and pattern recognition* (2016), pp. 770–778.
21. F. Safir, N. Vu, L. F. Tadesse, K. Firouzi, N. Banaei, S. S. Jeffrey, A. A. E. Saleh, B. P. T. Khuri-Yakub, J. A. Dionne, Combining Acoustic Bioprinting with AI-Assisted Raman Spectroscopy for High-Throughput Identification of Bacteria in Blood. *Nano Lett.* **23**, 2065–2073 (2023).
22. A. Zyubin, A. Lavrova, O. Manicheva, M. Dogonadze, V. Belik, I. Samusev, Raman spectroscopy reveals *M. tuberculosis* strains with different antibiotic susceptibility. *Laser Phys. Lett.* **16**, 085602 (2019).
23. V. R. Bollela, E. I. Namburete, C. S. Feliciano, D. Macheque, L. H. Harrison, J. A. Caminero, Detection of *katG* and *inhA* mutations to guide isoniazid and ethionamide use for drug-resistant tuberculosis. *Int. J. Tuberc. Lung Dis.* **20**, 1099–1104 (2016).
24. H. Li, H. Soto-Montoya, M. Voisin, L. F. Valenzuela, M. Prakash, Octopi: Open configurable high-throughput imaging platform for infectious disease diagnosis in the field, , doi:10.1101/684423.

25. H. Li, D. Krishnamurthy, E. Li, P. Vyas, N. Akireddy, C. Chai, & M. Prakash, Squid: simplifying quantitative imaging platform development and deployment. *bioRxiv*, (2020)
26. H. Li, F. Safir, E. Tae, B. Ogunlade, A.E. Saleh, J. Dionne, M. Prakash, Squid-Raman: democratizing Raman imaging. (in preparation).
27. J.-Y. Lim, J.-S. Nam, S.-E. Yang, H. Shin, Y.-H. Jang, G.-U. Bae, T. Kang, K.-I. Lim, Y. Choi, Identification of Newly Emerging Influenza Viruses by Surface-Enhanced Raman Spectroscopy. *Anal. Chem.* **87**, 11652–11659 (2015).
28. R. Adato, A. A. Yanik, J. J. Amsden, D. L. Kaplan, F. G. Omenetto, M. K. Hong, S. Erramilli, H. Altug, Ultra-sensitive vibrational spectroscopy of protein monolayers with plasmonic nanoantenna arrays. *Proc. Natl. Acad. Sci. U. S. A.* **106**, 19227–19232 (2009).
29. M. Bhamidipati, H.-Y. Cho, K.-B. Lee, L. Fabris, SERS-Based Quantification of Biomarker Expression at the Single Cell Level Enabled by Gold Nanostars and Truncated Aptamers. *Bioconjug. Chem.* **29**, 2970–2981 (2018).
30. I. Y.-C. Ou, J. A. Webb, C. M. O'Brien, I. J. Pence, E. C. Lin, E. P. Paul, D. Cole, S.-H. Ou, M. Lapierre-Landry, R. C. DeLapp, E. S. Lippmann, A. Mahadevan-Jansen, R. Bardhan, Diagnosis of immunomarkers in vivo via multiplexed surface enhanced Raman spectroscopy with gold nanostars. *Nanoscale.* **10**, 13092–13105 (2018).
31. R. Zhang, Y. Zhang, Z. C. Dong, S. Jiang, C. Zhang, L. G. Chen, L. Zhang, Y. Liao, J. Aizpurua, Y. Luo, J. L. Yang, J. G. Hou, Chemical mapping of a single molecule by plasmon-enhanced Raman scattering. *Nature.* **498**, 82–86 (2013).
32. N. R. Jana, L. Gearheart, C. J. Murphy, Wet Chemical Synthesis of High Aspect Ratio Cylindrical Gold Nanorods. *J. Phys. Chem. B.* **105**, 4065–4067 (2001).
33. P. K. Jain, K. S. Lee, I. H. El-Sayed, M. A. El-Sayed, Calculated absorption and scattering properties of gold nanoparticles of different size, shape, and composition: applications in biological imaging and biomedicine. *J. Phys. Chem. B.* **110**, 7238–7248 (2006).
34. Lin, K.-Q, J. Yi, S. Hu, B.-J Liu, J.-Y Liu, X. Wang, and B. Ren, Size Effect on SERS of Gold Nanorods Demonstrated via Single Nanoparticle Spectroscopy. *J. Phys. Chem. C.* **120**, 20806–20813 (2016).
35. X. Ye, C. Zheng, J. Chen, Y. Gao, C. B. Murray, Using binary surfactant mixtures to simultaneously improve the dimensional tunability and monodispersity in the seeded growth of gold nanorods. *Nano Lett.* **13**, 765–771 (2013).
36. K. C. Carroll, M. A. Pfaller, M. L. Landry, A. J. McAdam, R. Patel, S. S. Richter, D. W. Warnock, *Manual of Clinical Microbiology, 2 Volume Set* (Wiley, 2019).

Acknowledgements:

The authors thank Chris Cundy, Ahmed Shuabi, Dr. Fareeha Safir, Dr. Jack Hu, Dr. Halleh Balch, and Liam Herndon for many insightful discussions. The authors thank Dr. Fareeha Safir for assistance with collecting SEM images of BCG, Liam Herndon for assistance with gold nanorod synthesis, and Ariel Stiber for assistance collecting TEM images of gold nanorods.

Funding:

- Stanford Catalyst for Collaborative Solutions (funding ID 132114)
- The Chan Zuckerberg Biohub Investigator Program
- The Gates Foundation (OPP 1113682)
- The National Science Foundation (grant number 1905209)
- The NIH New Innovator Award (1DP2AI152072-01).
- Part of this work was performed at the Stanford University Nano Shared Facilities and Stanford University Nanofabrication Facilities, which are supported by the National Science Foundation and National Nanotechnology Coordinated Infrastructure under awards ECCS-2026822 and ECCS-1542152 as well as the Stanford University Cell Sciences Imaging Core Facility.

Author contributions:

- Conceptualization: LFT, AAES, BO, HL, AKB, MP, JAD
- Methodology: LFT, BO, HL, AAES, NV
- Investigation: BO, HL, LFT
- Formal Analysis: BO, NV, HL
- Visualization: BO
- Funding acquisition: JAD, AKB, MP
- Resources: JAD, AKB, MP, NB
- Writing – original draft: LFT, BO, HL, AAES, JAD
- Writing – review & editing: LFT, BO, HL, AKB, NV, JAD

Competing interests:

The authors declare that they have no competing interests.

Data and materials availability:

All data needed to evaluate the conclusions in the paper are present in the paper and/or the Supplementary Materials. Additional data related to this paper may be requested from the authors.

Supplementary Information: Predicting tuberculosis drug resistance with machine learning-assisted Raman spectroscopy

Materials and Methods:

BACTERIAL STRAINS

To raise antibiotic resistant mutants, BCG was plated on 7H10 media with increasing concentrations of each antibiotic of interest. Plates were incubated at 37 °C for 21 days. Individual colonies were selected and grown in 7H9 media containing OADC, 0.2% glycerol, and 0.05% Tween-80; antibiotic resistance was confirmed by Minimum inhibitory concentration (MIC) testing.

MIC DETERMINATION

Each strain was grown to mid-log phase in 7H9 media containing OADC, 0.2% glycerol, and 0.05% Tween-80. Cultures were then diluted back to an OD600 of 0.01 in media containing 2-fold dilutions of each antibiotic of interest. Cultures were grown at 37°C in 96-well plates; bacterial cells were mixed at 7 and 14 days of incubation, and growth was determined by OD600 measurements on a Tecan Spark plate reader.

BACTERIAL PREPARATION FOR SPECTROSCOPY

To obtain the antibiotic-resistant BCG strains, wildtype BCG (ATCC 35737 TMC 1019 [BCG Japanese]) was grown to mid-log phase in 7H9 liquid media supplemented with OADC, glycerol, and tween-80, then pelleted and plated on 7H10 solid media containing serial dilutions of each antibiotic of interest from 10-fold above the MIC to 10-fold below the MIC. Plates were incubated at 37 °C for 4 weeks; individual colonies were then selected for subculture. Particularly, each colony harbors a unique resistance gene and hence was used as a sub-strain for the specific resistance pattern that we studied. To determine MIC, wild-type BCG and each resistant strain was grown to mid-log phase, then diluted back to an OD600 of 0.01 and incubated in two-fold serial dilutions of each antibiotic in a 96-well plate. Days 7 and 14 post-inoculation, each well was gently mixed and OD600 was read on a TECAN Spark device. Only confirmed resistant mutants, as well as the fully-susceptible (wildtype) strains were used for Raman testing. 1 mL of frozen stock of the wildtype and the confirmed resistant mutants were seeded in 10 mL 7H9 liquid media supplemented with OADC, glycerol, and tween-80 and incubated at 37 °C shaking at 115 RPM until mid-log phase (~5-6 days) using the Thermo Scientific MaxQ 4450 incubator. Cultures were then chemically inactivated overnight in a 1:1 solution using 10% formalin. 1.5 mL of culture (~4 *10⁸ cells/mL) was washed with water three times at 6000 rpm for 4 min using a mySPINTM 6 Mini Centrifuge. The BCG strains were prepared for Raman interrogation by resuspending the final washed pellet in 100 µL of sterile water and drying 3 µL of the suspension on a gold-coated silica substrate. Droplets were dried for 20 minutes and Raman was collected immediately after drying.

For the sputum spiked BCG Raman interrogation, 25 μL of 3x washed bacteria was spun down and resuspended in 50 μL of sputum. After sitting for 1 minute, the spiked sputum was then spun down, washed once with DI water, and then resuspended in 25 μL of DI water. 5 μL of cell solution was mixed with nanorods in a 1:1 ratio, and 3 μL of the suspension was dried on a gold-coated silica substrate.

RAMAN SPECTRAL DATA COLLECTION AND PROCESSING

The BCG strains were illuminated with a 633 nm laser powered at 13.17 mW. The Raman spectra were collected from 742 cm^{-1} to 1802 cm^{-1} using a 100x, 0.9 NA objective with a spot size of $\sim 1.5\text{ }\mu\text{m}$, a 600 l/mm grating, and 15 second acquisition time per spectra, ensuring that spectra are collected from single to at most a few bacterial cells at a time. Python (Jupyter Notebook) was used to process spectral data. Individual spectra were smoothed using wavelet denoising, specifically using the denoise wavelet function from the scikitimage Python library. Background was then subtracted using a polynomial fit with degree 5, and spectra were individually normalized to have zero mean and unit variance across all wavenumbers.

GOLD NANOROD PREPARATION FOR SERS MEASUREMENT

Hexadecyl(trimethyl)ammonium bromide (CTAB) and sodium oleate (NAOL) coated gold nanorods were synthesized following previously described protocol (31). The nanorods were cleaned by centrifuging 1 mL aliquots once at (9000 rpm, 20 min) and were concentrated down to 50 μL volumes. Nanorods were mixed with bacteria in 1:1 volumetric ratio to enable uniform coating as described in our earlier work (8). Absorption spectra were recorded using a Cary 5000 UV-vis-NIR spectrometer. Scanning electron microscopy images were taken using FEI Magellan 400 XHR Scanning Electron Microscope and the Zeiss Sigma Scanning Electron Microscope (SEM). Transmission electron microscopy images were taken using FEI Tecnai G2 F20 X-TWIN Transmission Electron Microscope (TEM).

CNN ARCHITECTURE AND CLASSIFICATION

Our CNN model is adapted from a ResNet (19) architecture, consisting of an initial convolutional layer with 64 filters, 7 residual layers, and one fully connected layer. Each residual layer consists of two residual blocks and each convolutional layer has 32 hidden nodes. We used a minibatch size of 32. To assess the classification performance, we used 10-fold cross validation, which splits the dataset into 10 equal stratified sets (Scikit-learn StratifiedKFold). For each fold i , we leave set i as the test set and train model i using all remaining data. Model i is then used to classify data in set i (test set). We repeat this process for all 10 folds, which produces unbiased classifications for all the data, and these are compared against the ground-truth to generate confusion matrices and the overall accuracy. All t-SNE projections were plotted using Scikit-learn manifold t-SNE with a perplexity = 15.

To determine the most important wavenumbers or spectral bands affecting classification performance, we used a probing algorithm that perturbs the input data before re-running the

classification through the trained models. Using the test fold from our 10-fold cross validation, we iterate through the wavenumbers and at each iteration, perturb the spectrum by modulating the amplitude of the spectral intensity with a Voigt distribution centered at the probing wavenumber. After each perturbation, we recalculate the classification accuracy, compare the updated results with our baseline classification accuracy, and determine the importance for each wavenumber - the greater the decrease in accuracy due to a given perturbation, the more important the wavenumber. Each wavenumber of each spectrum in the test fold is perturbed 5 times by randomly sampling spectral intensity values at that wavenumber in order to create random, but spectrally sensible instances. Finally, all results are averaged to determine our final feature importance.

DATA COLLECTION ON OCTOPI-RAMAN

Raman spectra were collected from 350 cm^{-1} to 1606 cm^{-1} using a 20x, 0.75 NA objective with spot size of 5.5 μm (Gaussian diameter; FWHM of 3.2 μm), laser power of 2.53 mW, and 0.3 second acquisition time per spectrum.

SPUTUM SAMPLES

To obtain processed sputum for Raman interrogation, sputum samples were decontaminated and concentrated per standard laboratory procedure (32) as follows: the sputum samples were treated with N-acetyl-l-cysteine-sodium hydroxide (NALC-NaOH) to break up the mucus and treated with NaOH to kill the oral flora. The pH was then neutralized with phosphate buffer and samples were concentrated with centrifugation. Only sputa with a negative acid-fast bacilli microscopy result (mycobacteria-negative) and from patients at low risk for TB were used for BCG spiking.

Figs. S1 to S7:

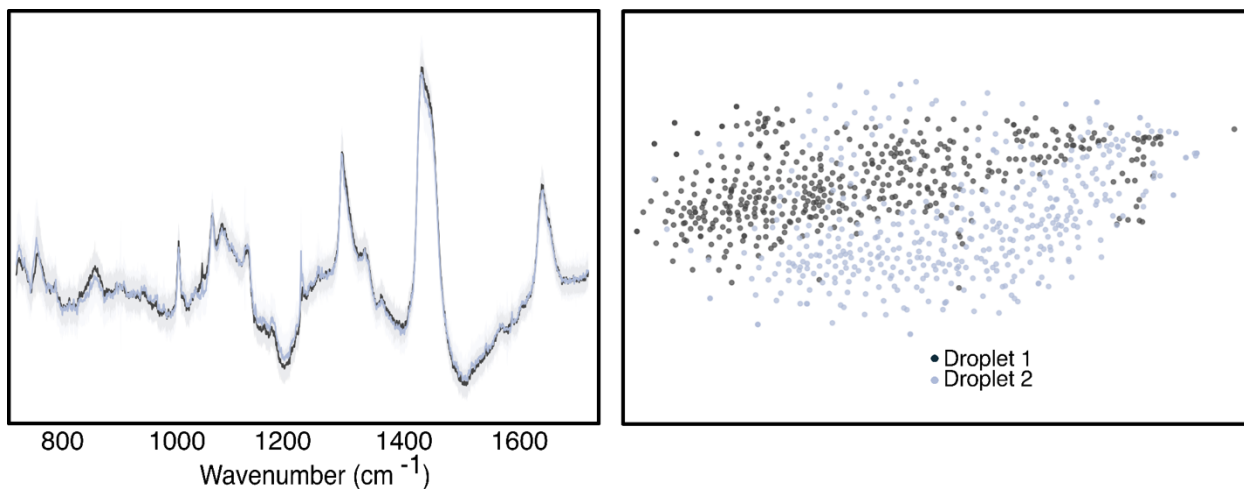


fig. S1. Droplet repeatability study. 450 Raman spectra of wildtype BCG collected on two separate droplets, showing spectral overlap and T-SNE overlap.

		Predicted	
		Isoniazid	Amikacin
True	Isoniazid	99	1
	Amikacin	1	99

fig. S2. Confusion matrix classifying the isoniazid and amikacin resistant mutants when grouped according to their antibiotic class, showing ~99% classification accuracy (529 spectra per strain; 2116 spectra for the Isoniazid grouping and 1587 spectra for the Amikacin grouping)

True	Predicted				
	Wildtype	Amikacin	Rifampicin	Isoniazid	Moxifloxacin
Wildtype	95			5	
Amikacin		97	1		2
Rifampicin	1	1	95	1	2
Isoniazid	5			94	1
Moxifloxacin		3	2		95

True	Predicted				
	Wildtype	Amikacin	Rifampicin	Isoniazid	Moxifloxacin
Wildtype	96			4	
Amikacin		98			2
Rifampicin	1	1	95	1	2
Isoniazid	5			95	
Moxifloxacin		4	2	1	93

fig. S3. Confusion matrices from two replicate studies on the Horiba Labram scientific grade Raman microscope showing an average of ~95% accuracy across the 5 BCG strains (~450 and 529 spectra per strain collected, respectively).

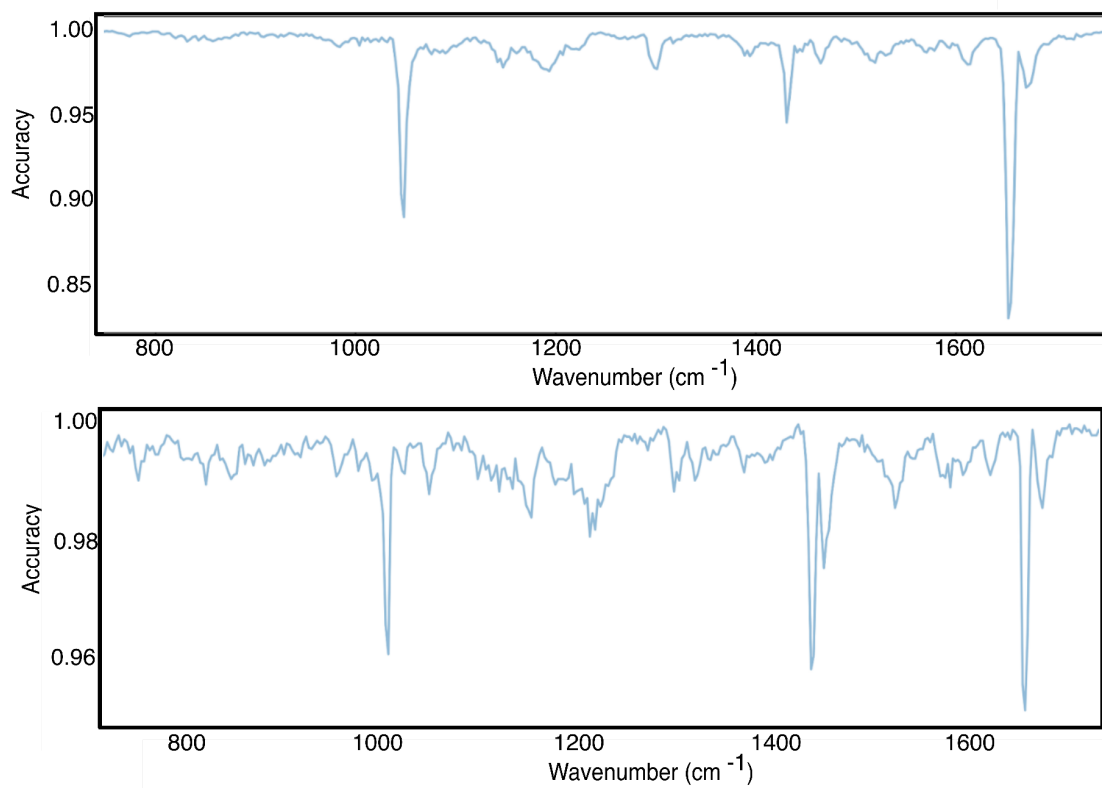


fig. S4. Feature selection from two replicate studies on the Labram.

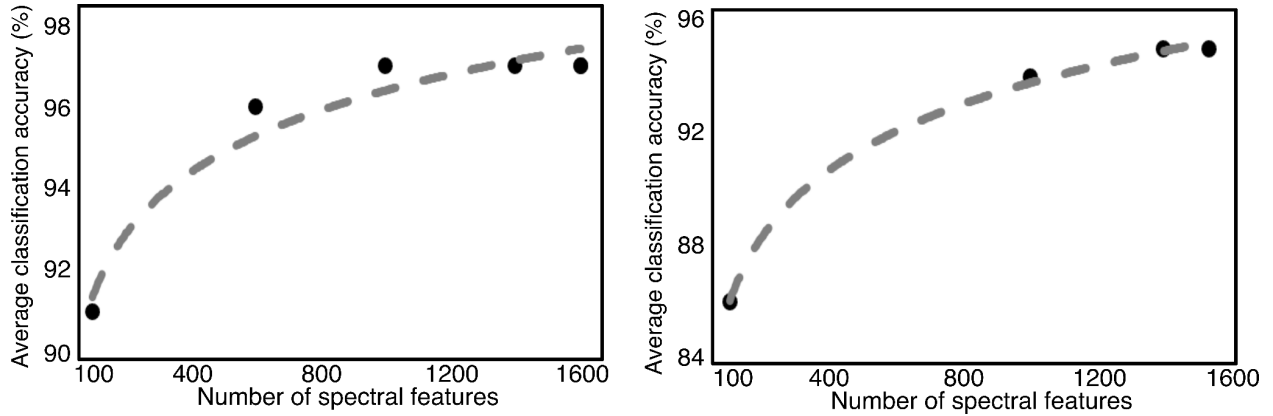


fig. S5. Average classification accuracy vs number of spectral features for two replicate Labram studies.

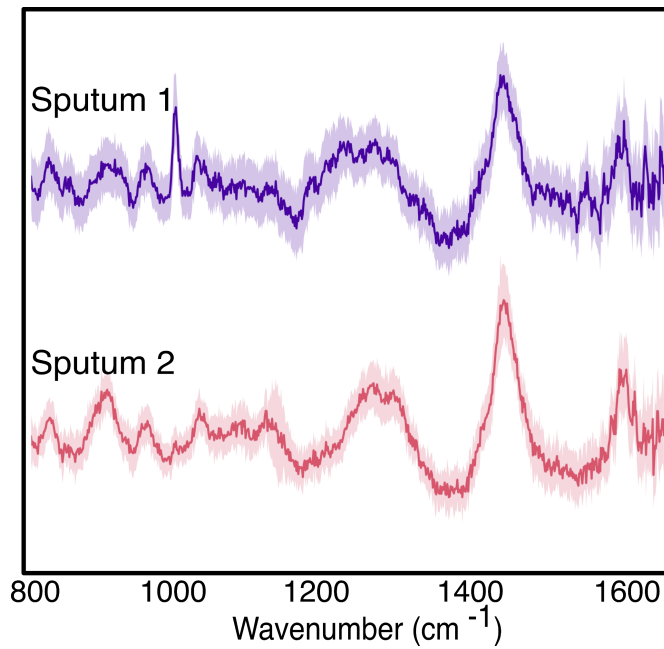


fig. S6. Average Raman spectra of the two sputum samples used in the Octopi study.

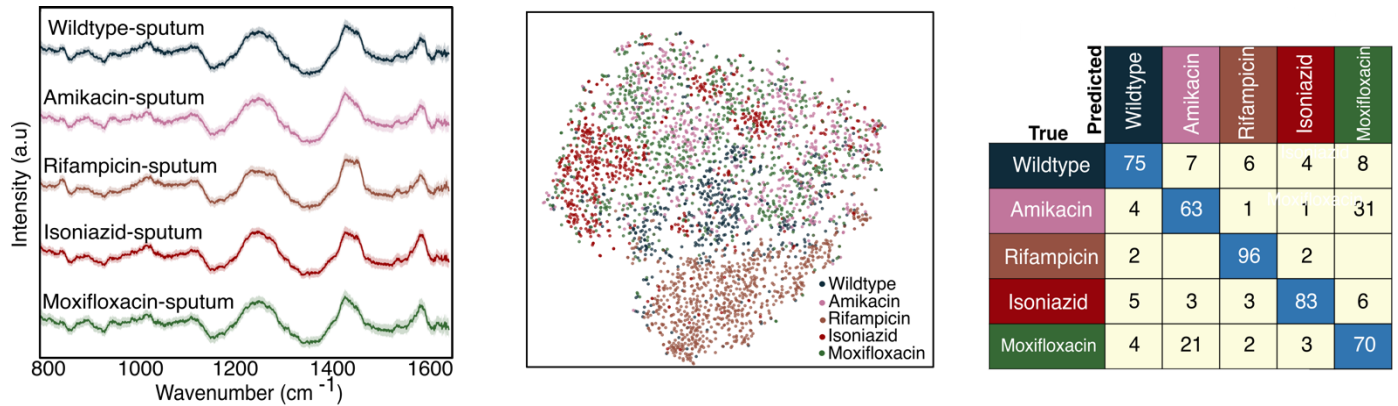


fig. S7. Mean Raman spectra of 5 BCG strains spiked in other sputum sample collected on Octopi-Raman with t-SNE showing some clustering by antibiotic class, and the confusion matrix demonstrating ~ 77% average classification accuracy.

Table S1:

Antibiotic	MIC ₉₀ ($\mu\text{g/mL}$)				
	Wildtype BCG	Amikacin-resistant BCG	Isoniazid-resistant BCG	Moxifloxacin-resistant BCG	Rifampicin-resistant BCG
Amikacin	0.0625	> 4.0	0.0625	0.0625	0.0625
Isoniazid	0.5	0.5	<1	0.5	0.5
Moxifloxacin	0.016	0.016	0.016	1	0.016
Rifampicin	<0.008	<0.008	<0.008	<0.008	<4.0

table S1: Minimum inhibitory concentrations of the five BCG strains studied. This was obtained using standard serial two-fold dilution method.

References (35, 36):

35. X. Ye, C. Zheng, J. Chen, Y. Gao, C. B. Murray, Using binary surfactant mixtures to simultaneously improve the dimensional tunability and monodispersity in the seeded growth of gold nanorods. *Nano Lett.* **13**, 765–771 (2013).
36. K. C. Carroll, M. A. Pfaller, M. L. Landry, A. J. McAdam, R. Patel, S. S. Richter, D. W. Warnock, *Manual of Clinical Microbiology, 2 Volume Set* (Wiley, 2019).